Chemical imaging of buried interfaces in organic-inorganic devices using FIB-TOF-SIMS

M. Tiddia*[1], I. Mihara[2], M.P. Seah[3], G.F. Trindade[4,6], F. Kollmer[5], C.J. Roberts[6], R. Hague[4], G. Mula[1], I.S. Gilmore[3] and R. Havelund[3]

(1) Università degli Studi di Cagliari, Dipartimento di Fisica S. P. 8 Km 0.700, 09042 Monserrato (CA), Italy

(2) Kuraray CO., LTD., 2045-1, Sakazu, Kurashiki, Okayama, 710-0801, Japan

(3) National Physical Laboratory, Hampton Road, Teddington, TW11 0LW, United Kingdom

(4) Centre for Additive Manufacturing, The University of Nottingham, Jubilee Campus, Nottingham, NG8 1BB, UK

(5) ION-TOF GmbH, Heisenbergstr. 15, 48149 Münster, Germany

(6) School of Pharmacy, The University of Nottingham, University Park, Nottingham, NG7 2RD, UK

Corresponding authors: Mariavitalia.tiddia@dsf.unica.it and ian.gilmore@npl.co.uk

Abstract

Organic-inorganic hybrid materials enable the design and fabrication of new materials with enhanced properties. The interface between the organic and inorganic materials is often critical to the device's performance and therefore chemical characterization is of significant interest. Since the interfaces are often buried, milling by focused ion beams (FIB) to expose the interface is becoming increasingly popular. Chemical imaging can subsequently be obtained using secondary ion mass spectrometry. However, the FIB milling process damages the organic material. In this study, we make an organic-inorganic test structure to develop a detailed understanding of the processes involved in FIB milling and SIMS imaging. We provide an analysis methodology that involves a "clean-up" process using sputtering with an Argon gas cluster ion source to remove the FIB induced damage. The methodology is evaluated for an additive manufactured encapsulated strain sensor containing silver tracks embedded in a polymeric material. We show a polymer-silver interface with a resolution of 440 nm and that the polymer contains a low level of silver particulates.

Keywords: *FIB, ToF-SIMS, Argon cluster, milling, polymer, hybrid interfaces, additive manufacturing*

1

Introduction

Organic/inorganic interfaces play an important role in many innovative technologies, including polymer electrolyte membrane fuel cells, dye-sensitized solar cells, and next-generation nanoelectronic devices which incorporate organic components alongside conventional conductors and semiconductors.[1,2,3,4,5] Another important example is the enabling technology of additive manufacturing (AM) which is at heart an interfacial problem where multiple layers of material are consecutively deposited to build up a physical 3D object from digital data. This interface challenge with AM will be further extended with emergence of the next-generation AM that seeks to combine both structural and functional materials together in a single entity. For future 3D-printed electronics, this will necessitate the co-deposition of both dielectric (organic) materials alongside conductive inorganics that will create complex organic-inorganic interfaces as both inter and intra layers.[6]

The design, fabrication and optimisation of such devices demand methods for characterizing the organic-inorganic interfaces. Since these interfaces are usually buried, techniques are required for these inter- and intra-layers that can access depths of tens of microns into these complex structures. The integration of a focussed ion beam (FIB) to mill away material and expose these buried interfaces for high-resolution scanning electron microscopy (SEM) has revolutionised the measurement capability.[7] Tomographic images can be created through sequential milling and imaging cycles with a spatial resolution approaching 1 nm in the plane of the SEM image and a slice thickness down to 3 nm.[7,8] Analytical capabilities are possible when combined with energy dispersive x-ray spectroscopy (EDX) for chemical imaging of elements and back scatter electron diffraction for crystal microstructure. However, the capability is limited for light elements such as lithium used in battery technologies, hybrid organic-inorganic materials such as perovskites and for organic materials.

Secondary ion mass spectrometry (SIMS) uses a focused ion beam to probe a surface causing atoms and molecules to be emitted in a process known as sputtering. A small fraction of this sputtered material is charged and is subsequently analysed in a mass spectrometer. Traditionally, this has been a time-of-flight (ToF) analyser but, more recently, a high-resolution Orbitrap spectrometer has been used.[9] The same approach, used successfully in dual beam FIB/SEM, may be used with SIMS. The use of FIB milling to access buried interfaces overcomes well-known limitations of traditional sputter depth profiling that result from material dependent sputtering yields and the presence of voids. This was demonstrated in early work by Satoh et al.[10] and Crow et al.[11] In both studies, a Ga^+ FIB was used to mill and map elemental distributions in integrated circuits. A few years later, using a serial milling approach, Tomiyasu et al.[12] and Dunn & Hull[13] showed the potential for FIB-SIMS tomography based on 3D reconstruction from sequences of SIMS images. FIB-SIMS tomography developed concurrently with, if not slightly ahead of, FIB/SEM but the use of the methodology has been very limited in

comparison. This, in part, could be due to the difficulty in extracting secondary ions for mass analysis from the surfaces cut at an angle to the average surface. However, in recent years ToF-SIMS instruments have been equipped with FIB to access buried interfaces, and ToF analysers have been integrated in SEM instruments for mass analysis.[14] The use of FIB in state-of-the-art ToF-SIMS instrumentation has proven powerful e.g., for multi-element tomography of solid oxide fuel cells[15,16,17] and the analysis of battery materials where ToF-SIMS imaging provided evidence of the dissolution of manganese from a $LiNi_{0.5}Co_{0.2}Mn_{0.3}O_2$ electrode.[18] These results are excellent but chemical degradation caused by the FIB and possible beam heating effects in materials could limit the usefulness of FIBs for preparation of inorganic-organic hybrid materials for SIMS imaging.[19] The many existing protocols for FIB preparation and tomography of organic samples are useful but, in general, do not address chemical degradation as they have been developed for electron microscopy rather than molecular analysis using a surface sensitive technique.

The chemical degradation causes the FIB-SIMS analysis of organic-inorganic hybrid materials to be challenging. Methods are needed to minimize or remove the FIB damage for successful FIB-SIMS analysis. Recent work by Iida et al. shows how organic material that has been damaged by a FIB may be removed using Ar^+ gas cluster ion beam (GCIB) sputtering.[20] Here, we present a study of FIB-SIMS using three different FIB sources Ga^+, Bi^+ and Bi_3^+. A simple inorganic-organic test device has been developed consisting of a regular pattern of polymer, either polystyrene (PS) or poly(methyl methacrylate) (PMMA), and silicon oxide. This is used to study and optimize the FIB-SIMS parameters and the FIB damage cleanup procedure. The effectiveness of the method is demonstrated in the study of the organic-metal interface of a prototype encapsulated strain sensor made by 3D inkjet printing and a Cu nanoparticulate deposited on poly(ethylene tephtahlate) (PET) via low power IR irradiation procedure.

Experimental Methods

Test device: Organic-inorganic test devices were made using a Long-Life™ MCP-10 microchannel plate (MCP) (Photonis, US) that are commonly used in ToF detection systems. The MCP (Figure SI.1) consists of a regular array of hexagonal close packed open tubes with 10 μm hole diameter and a centre-to-centre separation of 12 μm. These holes are tilted at 12° to the surface normal. The MCP is made from glass tubes sintered together with a rubidium-containing Nichrome coating for secondary electron emission. The holes are subsequently filled with either PS or PMMA using a 4-step procedure described by Steinhart et al.[21]

The MCP was degreased in a bath of 20% nitric acid (Sigma-Aldrich, UK) for more than 24 hours and subsequently rinsed with purified water and acetone (Sigma-Aldrich, UK). The dried MCP was placed in a glass petri dish and the surface of the MCP was covered with powdered polystyrene (molecular

weight 2430, Sigma Aldrich, UK) or PMMA (molecular weight 340000, Sigma Aldrich, UK). A metal weight of 500 g was placed on the polystyrene. Keeping this arrangement, the polymer was annealed to 200 °C for 5 h in a vacuum allowing the polymer to melt and fill the channels in the MCP (see the scheme process in Figure SI.1)

3D inkjet printed organic-inorganic sample: A prototype encapsulated strain sensor containing silver tracks embedded in a polymeric material was manufactured by 3D inkjet printing of two different inks. The organic ink is made in-house and based on tri (propylene glycol) diacrylate (TPGDA) and the silver nanoparticle ink was purchased from Advanced Nano Products (SilverJet DGP-40LT-15C). Both polymer and silver layers were printed and cured/sintered contemporaneously by a LED-based UV source connected to the print-heads of a PixDro LP50 printer. More details of the ink formulations and printing process are described elsewhere.[22] The analysed volume of the sample contains, from bottom to top, 15 layers of polymer, 10 layers of silver and 5 layers of polymer. Based on previous studies, each polymer layer is approximately 10 µm thick and each silver layer is between 300 nm and 700 nm thick.

Low temperature sintering of Cu nanoparticulate: The Cu on PET sample was produced using a novel printing technique that utilises a low-power, focused IR laser to selectively irradiate metallic nanoparticulate loaded slurries. Using the widely known phenomena of low-temperature sintering of nanoparticulates, the laser irradiation causes the nanoparticulates – Cu in this case – to consolidate at a lower temperature than would be expected for the bulk materials. Though this approach shows promise as 3D printing process, this particular sample demonstrates the potential for use within flexible 2D printed electronics, hence the use of a flexible insulating substrate (PET). Using such a method shows the potential of achieving high resolution conductive tracks in an affordable and industrially acceptable material. It is therefore important to understand the inorganic/organic interface to assess aspects such as adhesion and conductivity of the tracks.

FIB-ToF-SIMS: In this study we use a TOF-SIMS 5 (ION-TOF GmbH, Germany). The ToF analyser is normal to the sample surface and it is equipped with a dual source ion column mounted at 45° to the sample surface. The dual source ion column provides a 20 keV Ar^+ GCIB or a 30 keV Ga^+ FIB ion beam aligned in the same direction. A liquid metal ion gun (LMIG) provides a Bi_n^+ analytical beam. This is also at 45° to the sample surface but is located at an azimuthal angle of 90° from the Ar^+ GCIB and Ga^+ column. Low energy electrons are used for charge neutralization and are provided by a flood gun delivering a current of 5 µA with an energy of 20 eV mounted at an angle of 57° to the sample normal. The secondary ion and electron imaging of the cross section are made using a mass-separated

1   30 keV Bi_3^{2+} beam in the high lateral resolution, "Fast Imaging", mode operating with the analyser in

2   delayed extraction mode. Using this condition, a spatial resolution of approximately of 200 nm is

3   achieved.[23,24] As already shown by Mihara et al.[25] this modality allows the minimization of topographic

4   effects to improve the detection of secondary ions from the crater wall.

5

6   **Cross-sectioning and clean-up:** To prepare a cross section for analysis, a Ga^+ FIB is used with an energy

7   of 30 keV and a current of 20 nA to mill out a crater that is 120 μm in the *x*-direction and 80 μm in the

8   *y*-direction as shown in Figure 1 (see Table 1 for the beam parameters). The milling is monitored using

9   the Bi_3^{2+} beam with a field of view of 200 μm by 200 μm containing 512×512 pixels. This configuration

10 is shown in Figure 1a with the Ga^+ FIB beam entering from the top of each image. The crater wall

11 prepared for SIMS imaging is the top wall, closest to the Ga^+ source, at an angle of approximately 45°

12 to the MCP surface normal. The beam follows a sawtooth raster pattern with the scan direction being

13 from left to right in the images, starting from the bottom and moving to the top in each scan as showed

14 in Figure 1b.

15
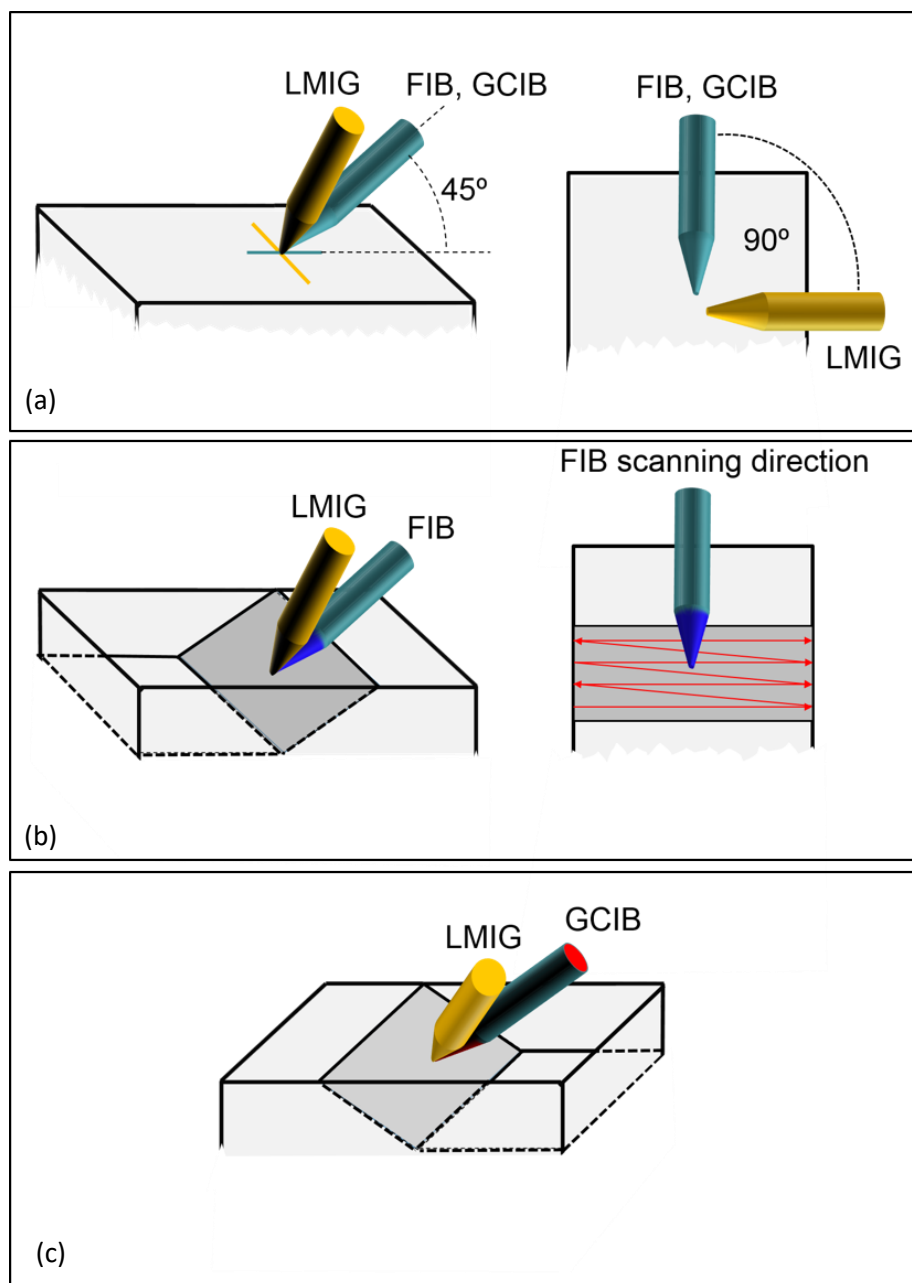
Figure 1. Schematic representation of the FIB-ToF-SIMS geometry. (a) FIB, LMIG, GCIB and sample orientations. (b) Sample milling orientation and FIB scan direction. (c) Cleaning process using the GCIB with a 180° rotation of the sample.

The sample is rotated 180° (see Figure 1c) for removal of the damaged layer on the FIB section using the Ar^+ GCIB. This clean-up procedure leads to the recovery of characteristic organic secondary ion signals from the milled wall (at approximately 45°, as we shall see later). The Ar^+ GCIB was an Ar_{2500}^+ beam at 10 keV (4 eV/atom) with a beam current of 6 nA and was rastered over a 500 μm × 500 μm area. Secondary ion images are recorded during the Ar^+ GCIB clean-up to follow the organic signal recovery using the Bi_3^{2+} beam with a current of 0.02 pA.

A further study to compare the effect of a bismuth source in the milling process is made by using the 3D OrbiSIMS (based on the TOF-SIMS 5 platform from ION-TOF GmbH, Germany) equipped with

1   a 30 keV bismuth LMIG with a Wien filter so that mass selected direct current beams of Bi^+ or Bi_3^+ can

2   be used.

Focused Ion Beam Parameters						
Type	Energy	Crater size	Current	Pixels in crater	Milling passes	Dwell time
Ga^+	30 keV	120 μm × 80 μm	20 nA	206 x 137	1, 2, 3	25 ms/pixel

3

4   *Table 1. FIB parameters used for the milling process.*

5

6   To optimize the lateral resolution of the secondary ion image, after the cleaning procedure, the sample

7   is further rotated 90º. In that orientation the Bi_3^{2+} beam is normal to the FIB section surface to give an

8   unhindered view of the cut surface.

9   **Results and discussion**

10   The recovery of characteristic polymer fragment ion signals from the 45° milled wall of both PS and

11   PMMA filled MCPs is shown as a function of the Ar^+ GCIB sputter dose in Figure 2. The characteristic

12   ion signal is seen to rise after a certain dose similar to that previously reported for ion and electron beam

13   damage.[26,27,28,29]

14

15   After FIB milling, a high Ga^+ signal is detected on the sloping surface and the organic signals are very

16   weak, presumably, due to polymer crosslinking and carbonisation. The damage provided by a FIB dose

17   of 4.08×10^4 ions/nm^2 was removed by approximately 10 ions/nm^2 of 10 keV Ar_{2500}^+ for PMMA and

18   60 ions/nm^2 for PS as shown in Figure 2. The faster recovery of the signal from PMMA is expected as

19   this polymer is not of the type that cross-links when exposed to ionizing radiation.[30]
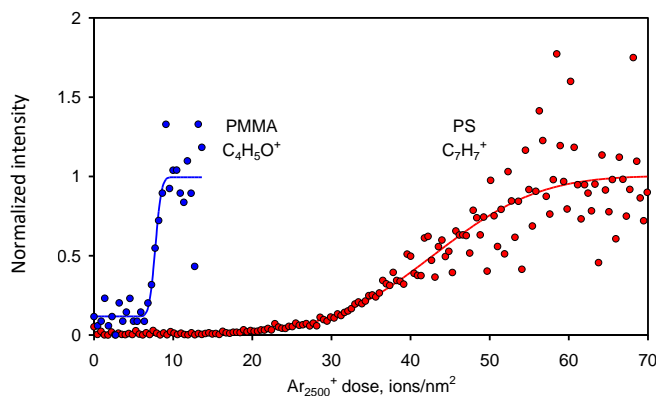
20   *Figure 2. Recovery of the intensity of characteristic fragment ions from PS ($C_7H_7^+$, red) and PMMA ($C_4H_5O^+$, blue)*

21   *during Ar^+ GCIB clean-up.*

In Figure 3a and 3b we observe, respectively, a SE image of the crater obtained providing a total dose of 4.09×10^4 ions/nm^2 for the MCP filled with PMMA and PS. Below, in Figure 3c and 3d we show the secondary ion images after the clean-up process for both filled specimens.


(a)

(b)

(c)

(d)
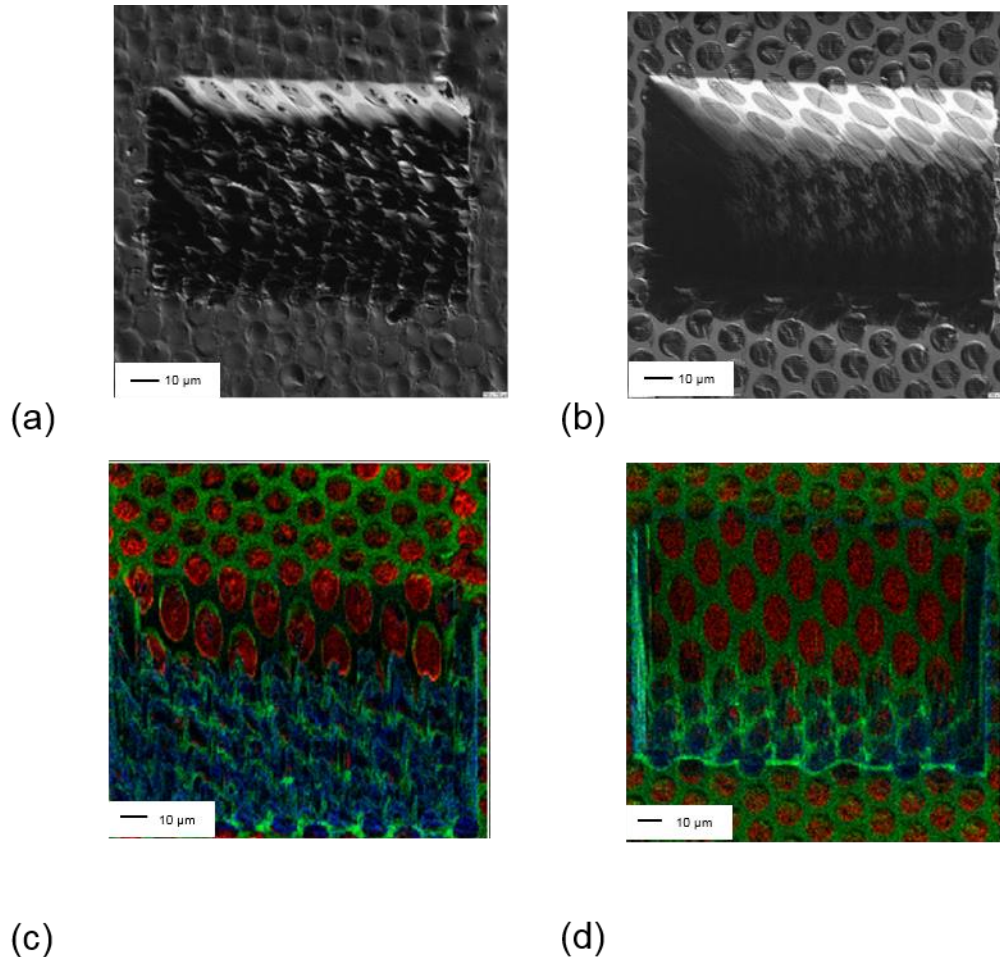
Figure 3. Secondary Electron (SE) in (a) and (b) and Secondary Ion (SI) in (c) and (d) images using the Bi_3^{++} ion beam of a crater milled into MCP test devices filled with either PS or PMMA. (a) SE image of MPC filled with PS and (b) similarly for PMMA. (c) SI overlay images of Rb^+ (green), Ga^+ (blue) and the characteristic PS fragment $C_7H_7^+$ (red) and (d) similarly for PMMA characteristic fragment $C_4H_5O^+$. Note that the imaging beam is at 45° to the MCP overall surface but the imaging system arranges the scan to a smaller deflection in its tilt direction to form a true square on horizontal surfaces. This causes the left hand vertical crater wall in (a) and (b) to appear to be sloping. Its opposite wall becomes hidden. Images (c) and (d) do not show this as the sample is rotated 90° for analysis and the images are rotated back that 90° for consistent presentation with (a) and (b).

FIB milling cutting procedure with Ga$^+$ using 1, 2 and 3 milling scans

Part of this work consisted of the observation of how the number of milling scans affect the milled depth and the required cleaning. By using 1, 2 and 3 milling scans, we linearly increase the Ga$^+$ beam dose. As a first step, we observe by optical microscopy how the milled depth develops in the case of the empty MCP matrix and in the case of the MCP matrix filled with PS (Figure SI.2). This increase of depth with dose appears to be near-linear and is very similar in the polymer-filled MCPs and in the

1 empty MCP since the sputtering of the polymer occurs at a higher rate than the sputtering of the

2 inorganic MCP.[31]
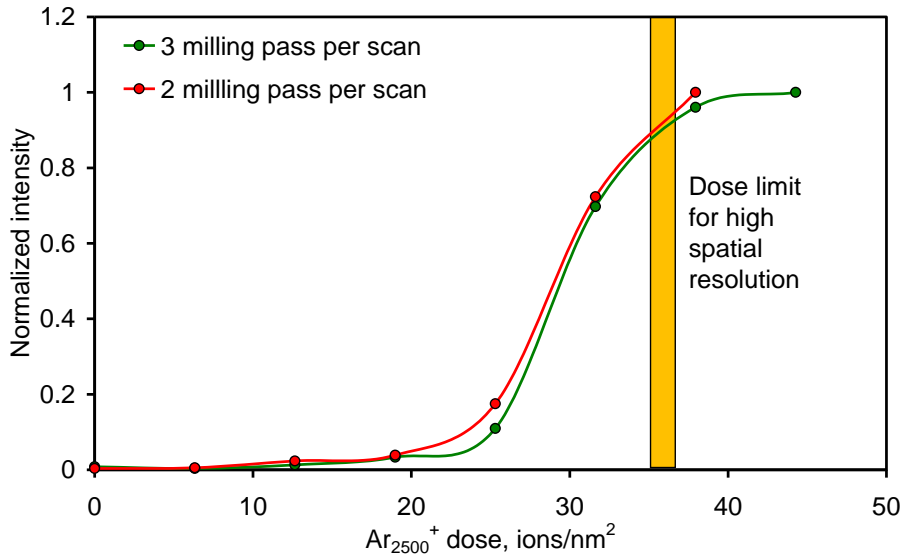
3

4 *Figure 4. $C_7H_7^+$ fragment signal recovery as a function of Ar^+ GCIB dose for 2 milling pass per scan and 3 milling pass*
5 *per scan FIB craters in the PS filled MCP. The yellow band shows the dose limit for retaining the highest spatial resolution.*
6

7 Figure 4 shows the clean-up at the crater wall (by selecting a region of interest centralized in the 45º

8 wall) formed by using 2 and 3 scans for the FIB milling. These craters are obtained by using the Ga^+

9 doses of 40900 ions/nm^2 and 61300 ions/nm^2. In cleaning the MCP, Figure 4 shows that a dose of 38

10 ions/nm^2 largely cleans the surface. In this geometry, the Ar^+ GCIB is normal to the surface. It is shown

11 elsewhere[32] that the sputtering yield of pure PS at 0° incidence, using 10 keV Ar_{2500}^+, is 21 nm^3.

12 However, in sputtering the Ga implanted PS, the yield is reduced to ~0.6 nm^3, a reduction of ~50 times

13 so that the 38 ions/nm^2 is what is required to remove the remaining 23 nm of damaged and implanted

14 PS.[32] If we were to overclean by a further 38 ions/nm^2, we should remove around a further 1 μm of pure

15 PS which would lead to blurring at the edges of included phases by significantly more than this figure

16 since the yield rises strongly at edges. Even if one limited the overclean dose to just 10%, the spatial

17 resolution would begin to be compromised. Different polymers are affected to different extents so that

18 the correct dose for both cleaning and retaining optimum spatial resolution will depend on the organic

19 material analysed. It is, therefore, recommended to measure the signals for the organic materials

20 anticipated in the sample and to stop the sputtering for imaging the sample at, or soon after, the signal

21 has reached 90-95% of its final value, as shown in Figure 4.

22

23 **Theory**

24

25 In the sputter shaping of materials, the angle dependence of the sputtering yield is critical. Wehner[33]

26 first showed the importance of this effect in the surface topography after sputtering. In 2012, Seah[34]

showed that good computations of surface form could be obtained by using a combination of Sigmund's sputtering theory[35] and the evaluations of relevant parameters by Yamamura et al.[36] Further evaluations were made by Seah[34] leading to a set of 9 equations to describe the sputtering yield and its dependence on the incidence angle, θ.

In the present work, we sputter using 30 keV Ga^+, 30 keV Bi^+ or Bi_3^+, or 10 keV Ar_{2000}^+. In the first case, we sputter unfilled MCPs. Their geometry gives a solid fraction of 0.37 for the SiO_2 of the MCP. The angle dependence of the sputtering yield for SiO_2 using 30 keV Ga^+ primary ions using Seah's equations [31] shows that the maximum yield occurs at $\theta_{max} = 80°$ (see Figure SI.3). Similar calculations for Ga^+ and Bi^+ and for energies in the range 10 keV to 50 keV give θ_{max} as 77° to 81° with slightly higher values for the lower mass primary ion and at the higher energies.

At 45° incidence to the MCP surface, the sputtering yield is 6.74 atoms/ion. In our 3 craters, we have used doses of 20400, 40900 and 61300 ions/nm^2 so we would expect depths of 4.8, 9.7 and 14.6 μm allowing for the 37% solid fraction. Actually, the depths measured by confocal microscopy are 13.5, 25.5 and 31 μm, some 2.4 times higher. The reason for this is that whilst the average MCP surface is at 45° to the beam, the local surface being sputtered is not at 45° to the beam. The sputtering is conducted as a raster scan where the beam has a profile, approximately Gaussian with a full width at half maximum of 0.8 μm on the sample surface and the pixel-to-pixel interval is 0.156 μm. Thus, the first application of the beam at 45° to the MCP surface digs a small hole but at the next pixel, there is an increased slope on the side being sputtered so the yield rises and a slightly deeper hole is made and so on until the angle of the FIB-milled slope at the side of the hole is approximately θ_{max}. It may locally increase beyond this value as a result of changes to other pixels. At 70° to the FIB-milled surface, the predicted vertical depths are 12.5, 25.1 and 37.7 μm, not very different from those observed using the confocal microscopy. The average angle of the beam to the FIB-milled surface may be less than θ_{max} since the sputtering takes some time to equilibrate and also the fringes of the beam are sputtering surfaces that are at lower angles, or it may be higher as discussed above. Thus, the measurements of the depth milled are broadly consistent with the model proposed. In Figure SI.4, we show AFM measurements on an unfilled MCP confirming that the FIB-milled slope angle starts at around 30° and rises to 40° as the depth from the MCP surface increases.

Note that here we have assumed an average solid fraction of 37% which would be valid if the holes were random. However, we can see in that the alignment of the holes means that, for the beam mid-way between the holes, the solid fraction is 100% whereas when aligned at the centres of the holes it is only 17%. This causes the unevenness observed of both the crater floor and the important back wall.

Calculations of the sputter profile using 30 keV Ga$^+$ on glass, at the final edge, are shown in Figure 5. These calculations are made with the beam orientated along the z-direction with columns of material along that direction and at the end, for presentation purposes the whole image is rotated 45° anticlockwise. The starred co-ordinate directions are in this rotated plane.
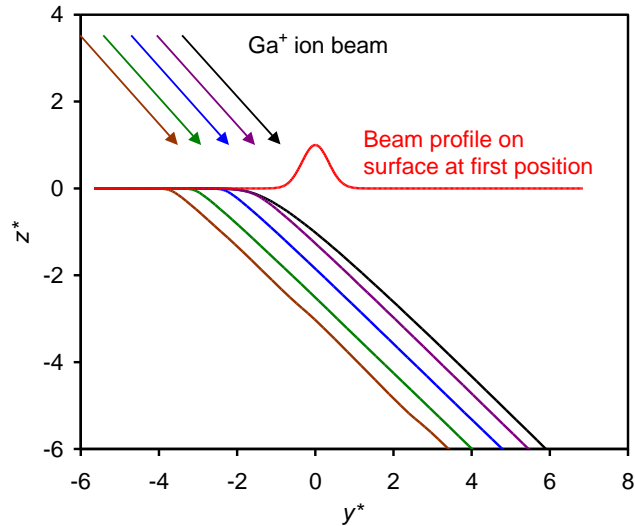
Figure 5. Calculations of the developing profile for 30 keV Ga$^+$ sputtering of glass at 45° incidence. The sputtering starts at y* = 0 and proceeds with many pulses at that position before moving 156 nm to the left and repeating the process many times. The beam profile is taken to be a Gaussian as shown but the precise shape is not important.

Could FIB milling with Bi$^+$ and Bi$_3^+$ be a useful alternative to Ga$^+$ for milling organic-inorganic hybrid materials?

Gallium is the most widely used source for FIB milling. Our 3D OrbiSIMS instrument also has a 30 keV bismuth liquid metal ion source equipped with a Wien filter so that mass selected direct current beams of Bi$^+$ or Bi$_3^+$ can be used, as mentioned in the experimental section. This provides an interesting possibility since cluster beams are known to create less damage in organic materials and therefore may be more suitable for inorganic-organic materials. Bi$^+$ and Ga$^+$ have much the same effect on glass in terms of the theory given above. To study the efficiency of these sources, we use the PS-filled test device. Figure 6 shows secondary electron images of craters with milling using Ga$^+$ (ToF-SIMS V) and Bi$_3^+$ (OrbiSIMS).
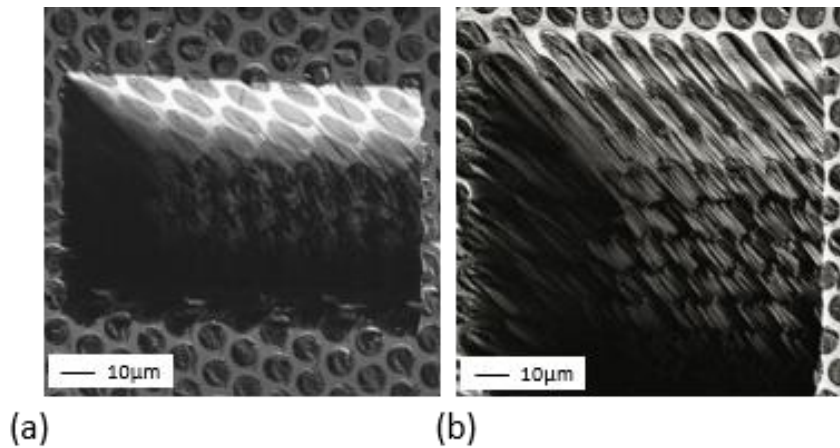
Figure 6. Emitted electron image using Bi$_3^{++}$ ions in the SIMS instrument of milled craters. (a) milled with Ga$^+$ and (b) milled with Bi$_3^+$. The sloping face is at the top. The left wall looks sloping but is vertical and this arises since the imaging beam comes from the right and the image surface geometry is "corrected" by expanding the x-direction by a factor of 2$^{0.5}$.

The results for Bi$^+$ (not shown) are very similar to, but poorer than, those for Ga$^+$. The results for Bi$_3^+$ are very much poorer and this arises partly due to the very different angular dependence of the sputtering of cluster ions compared with monatomic ions[37,38]. The value of θ_{max} for Bi$_3^+$ is much lower than for Ga$^+$ as the ions do not penetrate so far or so linearly. This leads to a slope closer to 30° with the ions no longer at the very grazing incidence into the polymer in the MCP holes shown in Figure SI.**5**. This allows a greater physical roughness to develop there and may explain the poor results for Bi$_3^+$.

 Observation of the columnar structure in each MCP hole using Bi$_3^+$ in Figure 6b would indicate that when using Bi$_3^+$ sputtering ions, some 2 to 3 μm of organic material may need to be removed to clean up the surface. If this were pure polystyrene, this would need the high dose of 70 ions/nm^2 for 10 keV Ar$_{2500}^+$, but if the removal of damaged polymer is one to two orders of magnitude slower[27,29, 32], this figure is raised by that factor and would be impossible to remove in a practical time. Clearly, the spatial resolution is very poor and the cleaning of the FIB section cut using Bi$_3^+$ may degrade that resolution further. It is therefore clear that the FIB-sectioning should be made with Ga$^+$.

Application of FIB-TOF-SIMS ~~to a 3D inkjet printed material~~

We applied FIB-TOF-SIMS to image the buried organic-inorganic interface of the 3D printed samples described in the experimental section. The two samples has been milled from the upper polymer part following the methodology described earlier.

 Figure 7 (a, b) shows the strain sensor and the total secondary ion images of the FIB crater after GCIB cleaning with a dose of 18.7 ions/nm^2 (Fig. 7c). Figure 7d shows a 45 μm x 45 μm map with an overlay of the signals for polymer ions and silver. After removal of the implanted gallium, the interface between the two materials is clearly distinguishable. To improve the signal to noise, an integrated intensity profile is created by summing the horizontal linescans between the regions indicated in Fig. 7d. Owing

to a tilt in the sample, a small horizontal offset is applied to each linescan to align them. Using the 16-84 % definition of profile resolution, the silver signal intensity across the interface (Fig. 7e) gives an organic-inorganic interface width as 440 nm. Above the interface, we see a small quantity of Ag. This could be interpreted as atomic diffusion whilst the overlayers are deposited or it could be from very small particles of Ag. Analysis of the SIMS spectra shows significant populations of Ag_3^+ and Ag_5^+ within the polymer, consistent with very small particulates, whilst none of the Ag adducts that would be expected for atomic or organically bonded Ag were observable. The populations are slightly smaller than for bulk Ag.
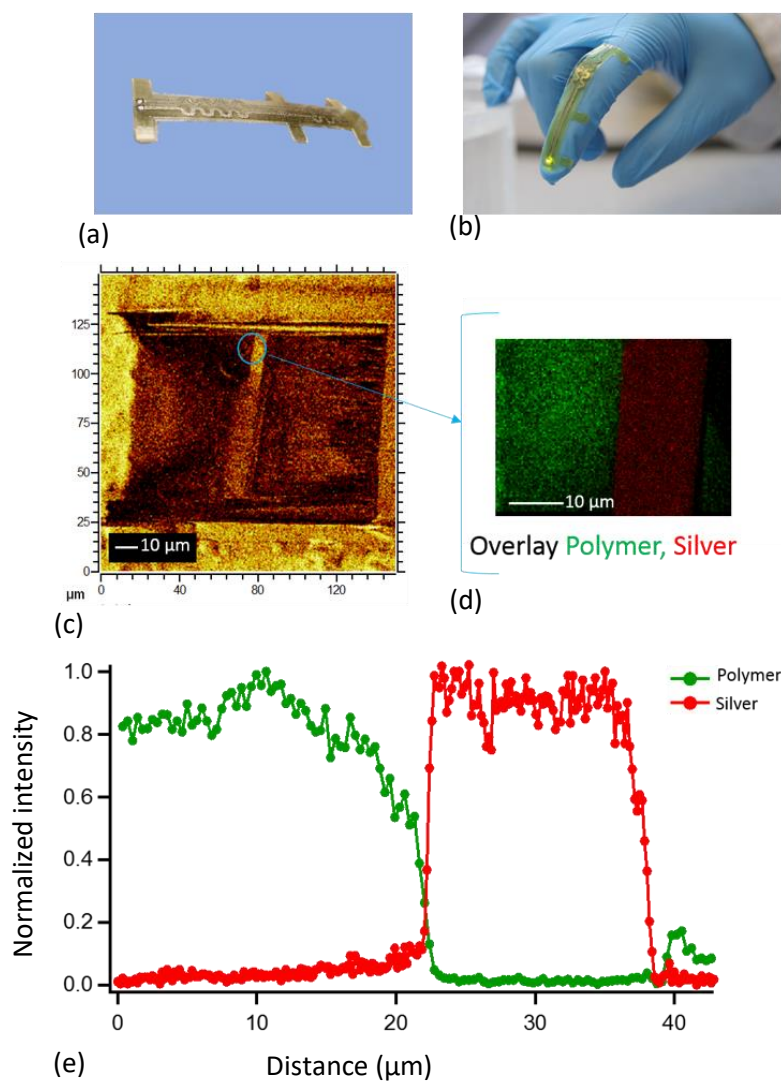
Figure 7. FIB-TOF-SIMS analysis of an additive manufactured encapsulated strain sensor. (a) Optical image of the sensor and (b) the sensor integrated with a disposable glove. (c) Total SI image of milled and cleaned crater. (d) High-resolution SI image of the interface with characteristic polymer fragment m/z 51 (green) and silver (the sum of Ag_3 and Ag_5) (red). Ag_1 is not used owing to mass interferences). (e) Normalized intensity profile of summed lines centred at the interfaces in (d).

Fig. 8 (a, b) shows the Cu nanoparticulate deposited on PET substrate and the schematic of the layer thikness. The sample has been milled with a Ga dose of 40900 ions/nm^2 and the characteristic PET fragment $C_8H_5O_3^+$ signal has been recovered with a dose of 12 ions/nm^2. In this specific case the interface has been determined in two steps: once the crater wall has been selected (see Fig. 8 c), the copper signal coming from CuO_2^+ ions has been recorded. Subsequently the Ar cluster cleaning, the PET fragment signal has been recorded from the same area selected in Fig. 8 (c) and the line profile of 125 summed lines cantered at the interface is shown in Fig. 8 (d). This approach permitted us to define a well interface also in the case of friable material.
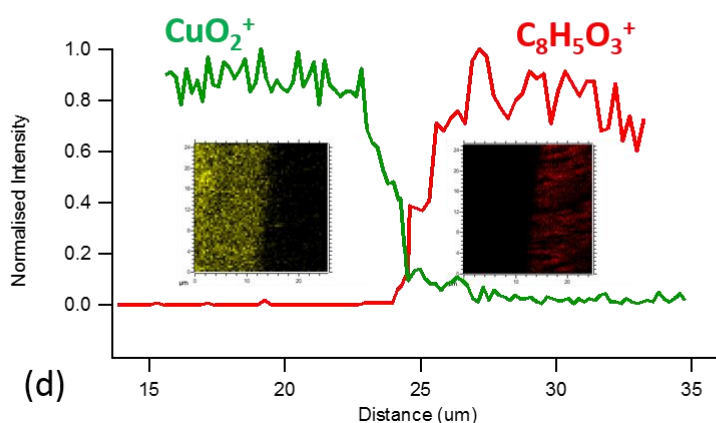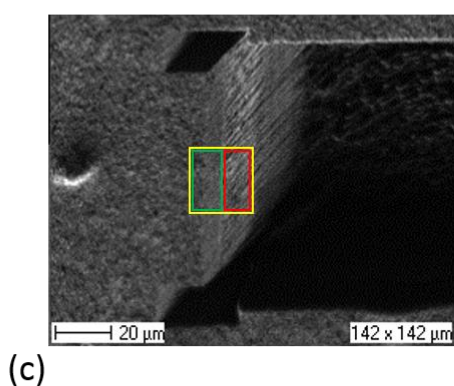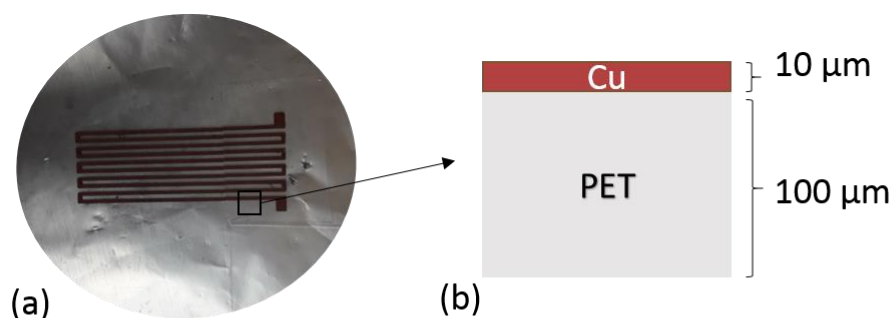
Figure 8. FIB-TOF-SIMS analysis of copper nanoparticulate layer on PET via low power IR irradiation. (a) Image of the device and (b) schematic of the layer depth.. (c) SE image of milled crater. Normalized intensity profile of summed lines centred at the interfaces in (d with incorporate the SI image from the characteristic signal of the Cu nanoparticulate in green and the PET fragment in red.

1

2

Conclusions

FIB-TOF-SIMS is a useful method for chemical imaging of buried interfaces. However, the FIB milling damages organic surfaces, which could limit the application for important organic-inorganic systems. We show that an Ar^+ GCIB clean-up cycle can remove this damage and provide essential information to do this effectively. We have developed a test device based on a microchannel plate consisting of a regular honeycomb array of tubes of 10 µm diameter in glass. The tubes are filled with either PMMA or PS. Using this device, we determine that 10 keV Ar_{2500}^+ doses of 10 ions/nm^2 and 60 ions/nm^2 are required to recover the organic signal for PMMA and PS, respectively.

We postulate that since Bi_3^+ has a higher sputtering yield than Ga^+ for organics, that the effects of damage on organics may be less. We use the test-device to evaluate this for FIB milling with 30 keV Ga^+, Bi^+ and Bi_3^+. We find, the reverse is in fact the case and explain this in terms of a theory based on the angular dependent sputtering yield. In this theory, the angle of incidence evolves from the initial 45º geometrical angle with the fresh surface to stabilize at near θ_{max} as the milling proceeds. Since θ_{max} differs substantially between atomic (approximately grazing) and cluster projectiles (approximately 45º) then the ability to successfully mill through materials with vastly different sputtering rates is affected. Therefore, gallium is recommended for milling organic-inorganic hybrid materials. We propose that the polymer filled MCP test device could have utility for FIB-TOF-SIMS interlaboratory comparisons to evaluate instrumentation and protocols and to improve reproducibility.

We apply the method to study the buried interface between a track of sintered silver nanoparticles and a UV-cured polymer in a 3D inkjet printed prototype encapsulated strain sensor. The two materials show a resolution at the interface of 440 nm. Above the interface is a very low level of Ag particulates.

1

Supporting Information. This shows the method of preparation of the polymer-filled MCP, details of the MCP craters as well as the AFM study to check the precise orientation of the sputtered plane of the sample, optical microscope images on empty and filled MCP, angular dependence on sputtering yield

Bibliography

(1)   Urban, J. J. One Model to Rule Them All. *Nat. Mater.* **2017**, *16* (2), 157–159.

(2)   Maurin, G.; Serre, C.; Cooper, A.; Férey, G. The New Age of MOFs and of Their Porous-Related Solids. *Chem. Soc. Rev.* **2017**, *46* (11), 3104–3107.

(3)   Breitwieser, M.; Klingele, M.; Vierrath, S.; Zengerle, R.; Thiele, S. Tailoring the Membrane-Electrode Interface in PEM Fuel Cells: A Review and Perspective on Novel Engineering Approaches. *Adv. Energy Mater.* **2018**, *8* (4), 1701257.

(4)   Freitag, M.; Teuscher, J.; Saygili, Y.; Zhang, X.; Giordano, F.; Liska, P.; Hua, J.; Zakeeruddin, S. M.; Moser, J. E.; Grätzel, M.; et al. Dye-Sensitized Solar Cells for Efficient Power Generation under Ambient Lighting. *Nat. Photonics* **2017**, *11* (6), 372–378.

(5)   Ali, Z.; Shakir, I.; Kang, D. J. Highly Efficient Photoelectrochemical Response by Sea-Urchin Shaped ZnO/TiO_2 Nano/Micro Hybrid Heterostructures Co-Sensitized with CdS/CdSe. *J. Mater. Chem. A* **2014**, *2* (18), 6474–6479.

(6)   EPSRC. EPSRC Programme Grant: Enabling Next Generation Additive Manufacturing http://gow.epsrc.ac.uk/NGBOViewGrant.aspx?GrantRef=EP/P031684/1 (accessed Aug 13, 2018).

(7)   Giannuzzi, L. A.; Stevie, F. A. *Introduction to Focused Ion Beams : Instrumentation, Theory, Techniques and Practice*; Springer, 2010.

(8)   Narayan, K.; Danielson, C. M.; Lagarec, K.; Lowekamp, B. C.; Coffman, P.; Laquerre, A.; Phaneuf, M. W.; Hope, T. J.; Subramaniam, S. Multi-Resolution Correlative Focused Ion Beam Scanning Electron Microscopy: Applications to Cell Biology. *J. Struct. Biol.* **2014**, *185* (3), 278–284.

(9)   Passarelli, M. K.; Pirkl, A.; Moellers, R.; Grinfeld, D.; Kollmer, F.; Havelund, R.; Newman, C. F.; Marshall, P. S.; Arlinghaus, H.; Alexander, M. R.; et al. The 3D OrbiSIMS—label-Free Metabolic Imaging with Subcellular Lateral Resolution and High Mass-Resolving Power. *Nat. Methods* **2017**, *14* (12), 1175–1183.

(10)   Satoh, H. Three-Dimensional Analysis of a Microstructure by Submicron Secondary Ion Mass Spectrometry. *J. Vac. Sci. Technol. B Microelectron. Nanom. Struct.* **1991**, *9* (5), 2638.

(11)   Crow, G. A.; Christman, L.; Utlaut, M. A Focused Ion Beam Secondary Ion Mass Spectroscopy System. *J. Vac. Sci. Technol. B Microelectron. Nanom. Struct.* **1995**, *13* (6), 2607.

(12)   Tomiyasu, B.; Fukuju, I.; Komatsubara, H.; Owari, M.; Nihei, Y. High Spatial Resolution 3D Analysis of Materials Using Gallium Focused Ion Beam Secondary Ion Mass Spectrometry (FIB SIMS). *Nucl. Instruments Methods Phys. Res. Sect. B Beam Interact. with Mater. Atoms* **1998**, *136–138*, 1028–1033.

(13)   Dunn, D. N.; Hull, R. Reconstruction of Three-Dimensional Chemistry and Geometry Using

1   Focused Ion Beam Microscopy. *Appl. Phys. Lett.* **1999**, *75* (21), 3414.

2 (14) Whitby, J. A.; Östlund, F.; Horvath, P.; Gabureac, M.; Riesterer, J. L.; Utke, I.; Hohl, M.;
3   Sedláček, L.; Jiruše, J.; Friedli, V.; et al. High Spatial Resolution Time-of-Flight Secondary Ion
4   Mass Spectrometry for the Masses: A Novel Orthogonal ToF FIB-SIMS Instrument with *In Situ*
5   AFM. *Adv. Mater. Sci. Eng.* **2012**, *2012*, 1–13.

6 (15) Hammond, J. S.; Fisher, G. L.; Bryan, S. R.; Kanarbik, R.; Möller, P. FIB-TOF Tomography of
7   Solid Oxide Fuel Cells. *Microsc. Microanal. 19* **2013**, *19* (2), 672–673.

8 (16) Kanarbik, R.; Moller, P.; Kivi, I.; Lust, E. Application of FIB-TOF-SIMS and FIB-SEM-EDX
9   Methods for the Analysis of Element Mobility in Solid Oxide Fuel Cells. *ECS Trans.* **2013**, *57*
10   (1), 581–587.

11 (17) PRIEBE, A.; GORET, G.; BLEUET, P.; AUDOIT, G.; LAURENCIN, J.; BARNES, J.-P. 3D Correlative
12   Morphological and Elemental Characterization of Materials at the Deep Submicrometre Scale.
13   *J. Microsc.* **2016**, *264* (2), 247–251.

14 (18) Börner, M.; Horsthemke, F.; Kollmer, F.; Haseloff, S.; Friesen, A.; Niehoff, P.; Nowak, S.;
15   Winter, M.; Schappacher, F. M. *Degradation Effects on the Surface of Commercial*
16   *LiNi0.5Co0.2Mn0.3O2 Electrodes*; 2016; Vol. 335.

17 (19) Seah, M. P. Cluster Ion Sputtering: Molecular Ion Yield Relationships for Different Cluster
18   Primary Ions in Static SIMS of Organic Materials. *Surf. Interface Anal.* **2007**, *39* (11), 890–897.

19 (20) Iida, S.; Carr, D. M.; Fisher, G. L.; Miyayama, T. Accurate and Reproducible In-Depth
20   Observation of Organic–inorganic Hybrid Materials Using FIB-TOF-SIMS. *J. Vac. Sci. Technol. B,*
21   *Nanotechnol. Microelectron. Mater. Process. Meas. Phenom.* **2018**, *36* (3), 03F107.

22 (21) Steinhart, M.; Wendorff, J. H.; Greiner, A.; Wehrspohn, R. B.; Nielsch, K.; Schilling, J.; Choi, J.;
23   Gösele, U. Polymer Nanotubes by Wetting of Ordered Porous Templates. *Science (80-.).*
24   **2002**, *296* (5575), 1997.

25 (22) Saleh, E.; Zhang, F.; He, Y.; Vaithilingam, J.; Fernandez, J. L.; Wildman, R.; Ashcroft, I.; Hague,
26   R.; Dickens, P.; Tuck, C. 3D Inkjet Printing of Electronics Using UV Conversion. *Adv. Mater.*
27   *Technol.* **2017**, *2* (10), 1700134.

28 (23) Vanbellingen, Q. P.; Elie, N.; Eller, M. J.; Della-Negra, S.; Touboul, D.; Brunelle, A. Time-of-
29   Flight Secondary Ion Mass Spectrometry Imaging of Biological Samples with Delayed
30   Extraction for High Mass and High Spatial Resolutions. *Rapid Commun. Mass Spectrom.* **2015**,
31   *29* (13), 1187–1195.

32 (24) Claus, T. K.; Richter, B.; Hahn, V.; Welle, A.; Kayser, S.; Wegener, M.; Bastmeyer, M.; Delaittre,
33   G.; Barner-Kowollik, C. Simultaneous Dual Encoding of Three-Dimensional Structures by Light-
34   Induced Modular Ligation. *Angew. Chemie Int. Ed.* **2016**, *55* (11), 3817–3822.

35 (25) Mihara, I.; Havelund, R.; Gilmore, I. S. Embedding-Free Method for Preparation of Cross-
36   Sections of Organic Materials for Micro Chemical Analysis Using Gas Cluster Ion Beam
37   Sputtering. *Anal. Chem.* **2017**, *89* (9), 4781–4785.

38 (26) Miyayama, T.; Sanada, N.; Bryan, S. R.; Hammond, J. S.; Suzuki, M. Removal of Ar+ Beam-
39   Induced Damaged Layers from Polyimide Surfaces with Argon Gas Cluster Ion Beams. *Surf.*
40   *Interface Anal.* **2010**, *42* (9), 1453–1457.

41 (27) Yamamoto, Y.; Ichiki, K.; Seki, T.; Aoki, T.; Matsuo, J. Ion-Induced Damage Evaluation with Ar
42   Cluster Ion Beams. *Surf. Interface Anal.* **2013**, *45* (1), 167–170.

43 (28) Havelund, R.; Seah, M. P.; Shard, A. G.; Gilmore, I. S. Electron Flood Gun Damage Effects in 3D

Secondary Ion Mass Spectrometry Imaging of Organics. *J. Am. Soc. Mass Spectrom.* **2014**, *25* (9), 1565–1571.

(29)   Kawashima, T.; Morita, H.; Fukumoto, N.; Kurosawa, T.; Aoyagi, S. Examination of Ion Beam Induced Damage on Polymer Surface Using Ar Clusters. *Surf. Interface Anal.* **2016**, *48* (11), 1175–1180.

(30)   Moore, J. A.; Choi, J. O. Degradation of Poly(Methyl Methacrylate); 1991; pp 156–192.

(31)   Seah, M. P. Universal Equation for Argon Gas Cluster Sputtering Yields. *J. Phys. Chem. C* **2013**, *117* (24), 12622–12632.

(32)   Tiddia, M.; Seah, M. P.; Shard, A. G.; Mula, G.; Havelund, R.; Gilmore, I. S. Argon Cluster Cleaning of Ga + FIB-Milled Sections of Organic and Hybrid Materials. *Surf. Interface Anal.* **2018**, DOI: 10.1002/sia.6522.

(33)   Wehner, G.; Gottfried. Influence of the Angle of Incidence on Sputtering Yields. *J. Appl. Phys.* **1959**, *30* (11), 1762–1765.

(34)   Seah, M. P. Topography Effects and Monatomic Ion Sputtering of Undulating Surfaces, Particles and Large Nanoparticles: Sputtering Yields, Effective Sputter Rates and Topography Evolution. *Surf. Interface Anal.* **2012**, *44* (2), 208–218.

(35)   Sigmund, P. Theory of Sputtering. I. Sputtering Yield of Amorphous and Polycrystalline Targets. *Phys. Rev.* **1969**, *184* (2), 383–416.

(36)   Yamamura, Y.; Itikawa, Y.; Itoh, N. *Angular Dependence of Sputtering Yields of Monoatomic Solids*; 1983.

(37)   Seah, M. P.; Spencer, S. J.; Shard, A. G. Depth Resolution, Angle Dependence, and the Sputtering Yield of Irganox 1010 by Coronene Primary Ions. *J. Phys. Chem. B* **2013**, *117* (39), 11885–11892.

(38)   Seah, M. P.; Spencer, S. J.; Shard, A. G. Angle Dependence of Argon Gas Cluster Sputtering Yields for Organic Materials. *J. Phys. Chem. B* **2015**, *119* (7), 3297–3303.